Research Square

Preprints are preliminary reports that have not undergone peer review.
They should not be considered conclusive, used to inform clinical practice,
or referenced by the media as validated information.

Surface Characterization of Laser Powder Bed Fusion for Melting Mode Determination

Sean D Dobson

sean4809@mit.edu

University of Cincinnati

Ashley E. Paz y Puente

Matthew A. Steiner

Research Article

Keywords: laser powder bed fusion, surface characterization, fast Fourier transform, melting behavior, metals, surface roughness parameters, relative density

Posted Date: December 9th, 2025

DOI: https://doi.org/10.21203/rs.3.rs-8117098/v1

License: This work is licensed under a Creative Commons Attribution 4.0 International License.
Read Full License

Version of Record: A version of this preprint was published at The International Journal of Advanced Manufacturing Technology on May 5th, 2026. See the published version at https://doi.org/10.1007/s00170-026-17820-4.

Abstract

The top surface of an additively manufactured part contains information about the most recently deposited layer but also preserves data about the layers preceding it. In laser powder bed fusion (L-PBF), the choice of process parameters significantly influences laser track consistency and impacts layer uniformity. As successive layers build upon each other, the surface becomes indicative of overall part quality, parameter effectiveness, and melting behavior. This research establishes key metrics that relate surface topology and melting behavior through comprehensive characterization of as-built L-PBF specimen surfaces using techniques that extend beyond simple summarization parameters like average roughness. Confocal laser scanning microscopy is employed to visualize 3-D height maps and quantify surface morphology using fast Fourier transforms (FFT). Furthermore, internal features are evaluated through relative density measurements obtained via metallographic methods, and microstructural analysis is conducted using electron backscatter diffraction. The results demonstrate the ability of surface features at different length scales to indicate part quality and melting behavior. FFTs are able to identify periodic surface characteristics, which correspond to high and low input energy melting, and can be used to distinguish between parts possessing similar summary surface parameters. Additionally, microscale laser path ripple angles are measured and shown to correlate to much broader process health metrics and melt pool behavior. The quantitative analysis employed using the FFT and laser path ripple angle provide novel methods for surface characterization that extend past the use of conventional summary parameters.

1. Introduction

In laser powder bed fusion (L-PBF) additive manufacturing (AM), laser parameters, such as laser power, scan speed, and hatch spacing, govern overall part quality [1]. Part quality can be determined using a number of metrics, the most common being relative density where > 99% equates to desirable properties [2]. It has been demonstrated previously that aspects of the surface topology can be linked to the relative density [3], [4]. Generally, as the mean surface roughness (R_a or S_a) improves, so does the relative density. While this is predominantly a correlative rather than causal relationship, particularly for the less extreme cases, the results demonstrate the capability to determine part quality by measuring readily available surface data non-destructively. However, summary parameters, such as S_a, do not provide a full description of a part's surface. Reducing a surface's topology to a single average roughness measurement completely neglects the shape, concavity, periodicity, feature density, and all roughness at a scale below the highest features observed. It is not surprising therefore that some specimens with similar S_a values can have vastly different relative densities. Characterization of morphological surface features in L-PBF such as the size and periodicity of defects, which may correlate better to metrics of concern, provide a more informative alternative to simpler roughness statistics such as S_a [5].

The surface features formed in the L-PBF process are attributed to the complex flow and melting behavior arising from laser-material interactions. When the laser beam interacts with the powder, sufficient energy induces a phase change, creating a molten liquid melt pool. The melt pool formed

experiences laser recoil pressure and thermocapillary convection, attributed to thermal and surface tension gradients [6], [7]. This causes the liquid to flow away from the incident beam location, termed Marangoni flow [8], resulting in oscillations in the melt pool [9]. Recoil pressure causes a depression in the melt pool that persists as the laser moves, due to metallic vapor plumes and gas plasma. Certain melt pool behaviors are linked to different melting modes [10]. In L-PBF, the primary melting modes include conduction, transition, and keyhole. Conduction mode results in a stable melt pool, yielding a quasi-semicircular track morphology [11]. However, stability in the melt pool doesn't always guarantee high-density parts. Factors such as surface tension often overcome recoil pressure in this mode, leading to non-uniform tracks and lack of fusion porosity [12], [13]. This mode is most associated with lower laser power and higher scan speeds and is typically outside the processing window for L-PBF materials. Transition mode represents the shift between conduction to keyhole modes, where the governing track forming mechanism changes from surface tension to recoil pressure. In this mode, the melt pool remains stable, exhibiting a quasi-semicircular track morphology, but the vapor depression is deeper compared to conduction, resulting in a conical shape [11]. Parameter sets exhibiting the transition mode can often lie within the high relative density process window. As power is increased or scan speed is decreased, the melting mode enters the keyhole mode, characterized by a deep and narrow vapor depression [14]. While the keyhole mode has a stable form in the high relative density process window, it also can be characterized by its unstable form whereby a deep vapor depression causes strong fluctuations that can result in depression collapse, leading to considerable splashing and the formation of both subsurface porosity and large scale surface roughness [14].

Surface roughness in L-PBF can be caused by multiple factors, including insufficient or excessive energy input during the process. Three key input parameters have been identified that affect surface roughness: laser power, scan speed, and hatch spacing [15]. To within certain limits, increased laser power can create a larger melt pool while smaller hatch spacing increases track overlap, promoting smoother surfaces. Proper scan speed is crucial for uniform tracks, as deviations from the optimal range can lead to melt pool instabilities. Understanding the combined effects of altered parameters is equally important. The volumetric energy density formula, though flawed, serves as a useful metric to explore these interactions. High volumetric energy density, corresponding to high power and/or low scan speed or hatch spacing, can lead to turbulent melt pools resulting in regions of large surface peaks and valleys in proximity [3]. Conversely, a lower volumetric energy density may cause insufficient energy where a lack of fusion surface forms and results in an inter-track undulation morphology with inadequate track overlap [16].

Several prior studies have characterized the top surfaces of L-PBF parts to gain a deeper understanding of their melting behavior. Mishra et al. [17] investigated the impact of base substrate surface morphology on the newly formed single track morphology. Their findings revealed that a uniform substrate leads to more coherent single laser tracks, whereas a non-uniform or rough surface results in melt pool irregularities. This implies that the parameters leading to lack of fusion or excessive splashing are generating a non-uniform surface for the next layer. This, in turn, affects the uniformity of the subsequent layer in a feedback loop. Similar effects are also found in other studies [18]. As non-uniform

layers continue to accumulate, a 'steady state' roughness is eventually reached, as demonstrated via *in situ* monitoring by Fleming et al. [19]. According to their findings, steady-state roughness is reached after approximately 30 layers. The final top surface therefore carries information about the morphology of several previous layers as well as the bulk of the part if the process parameters are being held constant.

This study comprehensively characterizes the surface of L-PBF specimens, going beyond conventional single value summary parameters. The primary goal is to discern distinct melting regimes and establish correlations between unique surface features and specific melting behavior by employing a fast Fourier transform (FFT) characterization method. The FFT approach has been previously utilized in a very limited manner to examine the surface roughness of L-PBF parts, where it was able to identifying periodic defects of a specific size but was not used to categorize melting behavior [20]. That specific study focused solely on using a single frequency associated with a particular defect, and the analysis was only performed on two specimens of the same material. In addition, FFTs have long been successful at identifying periodic surface features that arise in non-additive mechanical processes [21], [22], [23]. This investigation involves multiple materials fabricated using identical parameters, allowing for material-specific artifacts versus those attributable to the L-PBF manufacturing process itself to be distinguished.

2. Methods and Materials

The specimens were fabricated using an EOS M290 L-PBF AM machine equipped with a 400-watt laser. Three metallic powders, CoCrMo alloy, Ni-based superalloy 718, and 17 – 4 PH stainless steel, were chosen for fabrication due to their extensive use in L-PBF and their significance in aerospace and medical industries. These materials were procured from commercial vendors, and their powder particles were argon (Ar) atomized, exhibiting a particle size distribution with D50 ranging from 15 μm to 45 μm. For the fabrication process, an Ar environment was used, employing a 90° rotation scanning strategy without contour. A constant layer thickness of 40 μm and a spot size of 80 μm were maintained throughout the fabrication process. Laser power, scanning speed, and hatch spacing were deliberately varied to investigate their effects on the quality of the fabricated specimens under different processing conditions. The specimens were designed as simple cuboid shapes with dimensions of 11 mm in the X-axis x 10 mm in the Z-axis x 9 mm in the Y-axis. X is aligned parallel to the recoating direction, Y is parallel to the recoater, and Z is parallel with the build direction. Data labelling follows this convention.

In this study, only the top surface of the specimen was observed, as this data is readily available during fabrication, and the primary goal of this work is to eventually retrieve such data *in situ*. A Keyence VK-X260K high-resolution confocal laser scanning microscope (approximately 0.5 μm in the XY and 1 μm in the Z, with a systematic uncertainty of ± 2%) was utilized for characterization. The microscope was equipped with a 50x objective to generate 3-D height maps of each specimen's center, with an observed area of approximately 1.5 x 1.5 mm. This approach allowed for the measurement of the specimen’s surface morphology at 'steady state' fabrication conditions. From the generated height maps, the S_a roughness metric was calculated through the Keyence software. Prior to calculating the roughness parameter, the height map is processed through a plane fitting function to align the point cloud onto a

uniform plane. This corrects for any tilt existing in the sample during scanning, as this can affect the S_a value. To determine periodic surface morphology, the point cloud obtained from the height maps was visualized using a 1-D fast Fourier transforms (FFT) generated by averaging the point cloud along the direction parallel to the laser path, as depicted in Fig. 1. Several specimens were also characterized using the Gelsight Mobile Series 2 tactile sensor, a rapid characterization tool that provides high-resolution height data of the full sample surface (approximately 0.5 μm in the XY and 7 μm in the Z). This sensor utilizes a specialized elastic membrane and a multi-camera perspective, enabling quick spatial data generation, on the order of seconds.

Laser path ripples were observed through higher magnification confocal laser scanning microscopy. The scan area of the height map measures approximately 350 μm along the y-axis and 485 μm along the x-axis. The laser ripple angle was measured for several specimens by loading the height map into a computer aided design (CAD) software and manually fitting a line to either side of the laser ripple path and measuring the angle of the intersection. The measurement was taken at the trailing edge of the melt pool ripple formation from the confocal images taken at the center of the specimens. Multiple measurements were taken to generate error bars. Several of the height maps were additionally waveform reduced to accentuate the laser ripple formations. This was completed in the Keyence File Analyzer software using the smoothing function with a high waveform reduction setting.

The internal properties of specimens were characterized via metallographic methods. Relative density was measured using light optical microscopy with a 10X objective, followed by a thresholding and pixel counting technique to assess the density. Additionally, several 17 – 4 PH stainless steel specimens were etched using Kalling's Reagent #2 and imaged using a light optical microscope to reveal microstructural features. Electron backscatter diffraction (EBSD) analysis was performed on a ZEISS EVO 15 scanning electron microscope equipped with an Ametek EDAX Apex EBSD detector. The EBSD data was then analyzed using the EDAX OIM8 data analysis software to obtain crystallographic information and grain orientation mapping.

3. Results

a. Surface features as a means to distinguish melting behaviors and part qualities

The CoCrMo specimens in Fig. 2 were produced with a constant VED parameter set design by proportionally changing the laser power and scan speed, parameter values are provided on left of the figure. A constant hatch spacing of 80 μm was used. The Gelsight surface images visualize the entirety of the top surface of each sample. In specimen (a), with lower laser power and scan speed settings, a rough surface is produced with large-scale multi-laser track protrusions in close proximity to valleys. This can be seen in the Gelsight height map for this specimen which contains a high density of large peaks spotted in red. The distinct multi-track protrusions are indicative of unstable melting, attributed to a low scan speed allowing time for the melt pool to experience strong fluctuations. This is substantiated by the large irregular pores observed in the associated cross-sectional micrograph. As laser power and

scan speed are increased, the surface becomes uniform as seen in specimen (b). Surface uniformity indicates process stability, verified with the high relative density observed in the cross-sectional micrograph. Finally, in specimen (c), when laser power and scan speed are further increased proportionally, surface roughness begins to increase. Multi-laser track protrusions are observed in the surface morphology but are not as severe as the lower parameter setting of specimen (a). The increased surface irregularities also corresponds to an uptick in porosity, though porosity remains much smaller in scale.

A confocal height map was generated at the center of each specimen, the approximate location of which is indicated by the dashed lines in Fig. 2, to provide a higher resolution assessment of surface topology than offered by the Gelsight system. This method allows for the generation of a point cloud of data, something the Gelsight technique is not yet able to accomplish, and the calculation of 1D-FFTs as described in Fig. 1. Taking a height map from the center allows for the observation of approximately 'steady state' conditions. It is notable that the area observed in the confocal height maps appears to be sufficient in capturing similar surface artifacts present across the entirety of the specimen surfaces.

The multi-track surface protrusions noted in specimen (a) are reflected by the 1D-FFT amplitude spikes between frequencies of 0.001 and 0.005. By taking the inverse of the spatial frequency at the various peaks, the size of the defects can be determined. The major peaks in the image measure defects with sizes ranging from 1,000 μm to 200 μm. While the FFT amplitude does not provide direct height measurements, it does indicate the scale of features that are most prominent in the height data. The amplitude of peaks observed in the FFT for specimen (b) are much lower than those of specimen (a), which is consistent with the much more uniform and lower height surface topology clearly seen in the height map. The only peak of appreciable amplitude is located near the frequency of 0.0125, the inverse of which corresponds to the 80 μm hatch spacing used. Specimen (c) has several peaks with frequencies attributed to both larger sized defects and the hatch spacing. It can be observed in the confocal height map that the individual laser tracks are protruding. The unique jagged laser track observed in specimen (c) formation is likely a unique mode near the transitional melt region where the VED is sufficient for melting, but the higher scan speed results in shallow melt pool causing the melt to bulge also known as the "humping" phenomena [24].

In Fig. 2, the surface condition can be readily discerned using either the FFT or a summarized metric such as the arithmetic mean height, S_a. Although the S_a value does not offer insights into the specific melting conditions, it serves as a differentiating factor for evaluating surface quality. The S_a values for specimens (a), (b), and (c) are recorded as 32.1 μm, 7.82 μm, and 15.37 μm, respectively. The lowest S_a value coincides with the highest relative density, just as the surface with the highest S_a value corresponds to the specimen exhibiting the lowest relative density. However, there are instances where similar summary parameter values are associated with significantly distinct surface conditions and part qualities, as evident in Fig. 3. These three CoCrMo specimens all have parameter sets that produce similar S_a measurements. Each specimen within 1 μm of the same S_a value. Nevertheless, the porosities observed in the corresponding cross-sectional micrographs exhibit divergent outcomes that differ

dramatically between specimens. The height maps reveal disparate melting behaviors among the specimens, despite their shared average roughness. Specimen (a) in Fig. 3 exhibits surface features similar to specimen (c) in Fig. 2. Conversely, topology data from Fig. 3 (b) depicts a characteristic conduction mode melting, commonly associated with lack-of-fusion, as evidenced by the semi-circular laser tracks, and pronounced troughs between those tracks. Lastly, Fig. 3 (c) illustrates more prominent peaks and troughs, accompanied by an absence of discernible laser tracks, attributable to the narrower hatch spacing.

In comparison to the S_a average roughness, FFT analysis proves to be a more effective method for discerning distinct characteristics among the specimens. The FFT of Fig. 3 specimen (a) exhibits peaks related to both the hatch spacing and larger scale fluctuations, similar to specimen (c) in Fig. 2. Figure 3 specimen (b) has only one high-amplitude peak, which corresponds to the track spacing and suggests conduction mode melting where morphological defects predominantly remain within individual tracks. The amplitude of this major peak as well as those spanning the lower frequency range, are notable higher than that of the specimen in Fig. 2 (b), resulting in a much larger scale of roughness and higher porosity. In the case of Fig. 3 specimen (c)’s FFT, pronounced peaks are evident at lower spatial frequencies corresponding to the large surface protrusions with no distinct peak at the hatch spacing frequency. Despite having indistinguishable surface summary parameters, the FFT is able to provide helpful differentiations between these surfaces and can be used to predict part qualities.

b. Surface features as a means to distinguish specimens with high relative density

The preceding section aptly demonstrates the FFT's capacity to differentiate between components exhibiting differing melting behaviors and relative densities, even in scenarios where these components display comparable surface roughness summary parameters. Although relative density stands as a pivotal metric for characterizing components, it's not the sole determinant. This section explores the correlation between various surface conditions and the fabrication parameters employed, and how to interpret the microstructural attributes that emerge within diverse materials with high relative densities. In this context, the term "high relative density" pertains to specimens possessing relative densities surpassing the 99% threshold, a common benchmark [2].

IN 718 specimens, showcased in Fig. 4, were generated with parameters that maintain a consistent VED, achieved by proportionally adjusting power and scan speed. The hatch spacing was held constant at 80 µm. All three specimens exhibit high relative densities ranging from 99.83% to 99.97%, values overlayed in the confocal height maps. The employed parameter sets fall well within the process window of the IN 718 material. S_a values, also overlayed in the height maps, mirror the high relative density trend, displaying low values. However, a comprehensive analysis of their height maps and FFTs brings clear distinctions among the three specimens and provides insight into the different melting behaviors. Large surface protrusions are captured at lower spatial frequencies for the two rougher specimens, Fig. 4 (a) and (c), while the different amplitudes at the hatch spacing frequency follow the track intensities observed for each sample. The most prominent hatch spacing amplitude peak corresponds to Fig. 4 (c)

which displays the unique transitional mode humping phenomenon previously observed in Fig. 2 and Fig. 3. Figure 4 (b) possesses the most uniform surface of the three specimens, with the corresponding FFT demonstrating lower amplitude peaks at frequencies below the hatch spacing frequency.

The EBSD maps in Fig. 4 confirm an Face-Centered Cubic (FCC) crystalline structure. All of the observed regions exhibit crystal growth aligned with the build direction in columnar formations the thickness of the track spacing. The maps pertaining to Fig. 4 (a) and (b) exhibit a slight misalignment of the samples within the microscope, where the build direction orientation is subtly rotated clockwise. Accounting for this discrepancy, all specimens exhibit similar crystallographic {001}<100> “cube” textures, with of one variant of the {001} planes aligning along the Z-axis build direction, and the others aligning to the y-axis and x-axis scanning directions. This texture has been found to arise when cubic metals are produced by L-PBF utilizing an x-y crosshatch scan strategy, due to a combination of preferred solidification growth directions and the heat flux geometries in this strategy [25], [26], [27], [28]. A multiples of random distribution (MRD) value of 1 corresponds to a density of planes oriented in a direction being equal to that expected by the randomly oriented powder distribution. Because of the limited number of grains sampled within an EBSD map, MRD values derived from EBSD have significant natural experimental variations on the order of one MRD, so there is no evidence of a significant difference in texture strength amongst the IN 718 specimens. While the strength of all the textures are similar, the distribution of non-cube elements are discernably less clustered near the < 001 > directions in Fig. 4 (a) compared to the other specimens, as seen by the spread in the reduced inverse pole figure. Cubic symmetry has been employed in the reduction of the inverse pole figures, reducing the experimental noise by plotting the same data over a smaller angular space and making alignment trends and weaker textures easier to analyze.

17 − 4 PH specimens were generated employing identical parameters to those used in Fig. 4 for IN 718, and the corresponding data is presented in Fig. 5. Relative densities for these specimens are slightly below those of the IN 718 specimens in Fig. 4, but remain above 99%. The lowest S_a value aligns with the highest relative densities, yet the S_a values for Fig. 4 (a) and (c) are considered to possess higher levels of roughness. This challenges differentiation between these two samples using S_a, echoing the trends observed in Fig. 3. The melting behavior and surface morphologies mirror those of the IN 718 specimens depicted in Fig. 4. Specifically, Fig. 5 specimen (a) exhibits an undulating surface with larger protrusions spanning multiple tracks with corresponding higher amplitude peaks at lower frequencies in the FFT. Figure 5 specimen (b) showcases the most uniform surface and features lower amplitude peaks at lower spatial frequencies and a distinct peak at the hatch spacing frequency. While Fig. 5 specimen (c) displays characteristic jagged hatch spacing morphology associated with the transitional melting mode corresponding to a higher amplitude peak at the hatch spacing frequency. Additionally, several lower frequency peaks are present, corresponding to large, raised areas on the specimen surface.

The EBSD maps for 17 − 4 PH in Fig. 5 exhibit analogous trends to those seen in Fig. 4 for IN 718, though the 17 − 4 PH steel has a Body-Centered Cubic (BCC) crystalline structure. The same {001}<100 > crystallographic cube texture observed in the IN 718 samples is present but is much weaker as

evidenced by the lower MRD values (note that the MRD scale bars used in each figure are different) and is very close to becoming un-textured. The alignment for these weaker textures is best seen in the reduced inverse pole figures. It is notable that Fig. 5 specimen (b) appears to display more coherent columnar growth compared to the other specimens, which both possess surfaces that indicate a higher level of instability. Despite having little difference in MRD values, orientation preference appears to strengthen with increased laser power and scan speed, evident from the coalescing intensity peaks on the reduced inverse pole figures.

The CoCrMo specimens presented in Fig. 6 were manufactured using identical parameters to those employed in Fig. 4 and Fig. 5, and the height maps and the FFTs reveal similar trends to the preceding materials. Figure 6 specimen (a) displays multi-track protrusions, as confirmed by the amplitudes at low frequencies found in the FFT. Figure 6 specimen (b) exhibits a more uniform surface with less pronounced multi-track protrusions. Track periodicity is reflected in the FTT at the 0.0125 μm^{-1} hatch spacing frequency. Figure 6 specimen (c) is the same specimen presented previously in Fig. 2 (c). A sequence of five CoCrMo specimens produced with the same VED value can be seen progressing from Fig. 2 (a) → Fig. 6 (a) → Fig. 2 (b) →6 (b) → 2/6 (c), where the transition between unstable and stable melting conditions is captured by changes in the corresponding FFTs.

The EBSD maps in Fig. 6 confirm the CoCrMo specimens possess the FCC crystalline structure expected for this alloy. Analogous to previous observations in IN 718 and 17 − 4 PH alloys, a moderate {001}<100 > crystallographic cube texture oriented along the build direction is present, evidenced by the pole and inverse pole figures. The crystallographic texture exhibits similar trends to both IN 718 and 17 − 4 PH as a function of processing parameters, where the MRD values are approximately constant within the measurement variability of EBSD, but a clear trend of greater general alignment can be observed in the reduced inverse pole figures with increasing laser power and scan speed. Notably, the Fig. 6 specimen (b) with more uniform surface characteristics has more defined laser track columns running vertically through the microstructure than the other two conditions.

The results presented in Figs. 4–6 examined differences between specimens within the high-density process window. However, laser power and scan speed are not the only commonly altered parameters. The IN 718 specimens depicted in Fig. 7 were both constructed utilizing the same laser power and scan speed of 160 W and 840 mm/s, respectively. The sole disparity between these two specimens is the hatch spacing selected. Specimen in the left column uses a 60 μm hatch spacing while the right column specimen employed an 80 μm hatch spacing. Notably, both specimens possess high relative densities and low S_a values. The 60 μm specimen showcases metrics of 99.99% relative density and 6.44 μm S_a, while the 80 μm specimen registers values of 99.97% relative density and 9.75 μm S_a. A comparison of the FFTs offers additional quantitative information that can be used to distinguish between the two specimen surfaces. The 80 μm specimen exhibits a marginally higher amplitude peak at lower frequencies that dominates the S_a value, but crucially, there is also a pronounced peak at the selected hatch spacing frequency that is absent from the 60 μm specimen.

The differences captured in the FFT between these ostensibly similar samples can importantly be linked to the interplay between the processing parameters and the resulting microstructures formed at different processing conditions beneath the surface. EBSD maps and pole figures for IN 718 specimens printed with two different hatch spacings are presented in Fig. 7. The second row of the figure presents maps of the XZ plane that includes the build direction, while the maps in the fourth row align with the XY plane perpendicular to the build direction. In the XZ plane the 80 μm hatch spacing specimen microstructure exhibits similar microstructural characteristics to the IN 718 specimens seen previously in Fig. 4. A cross-hatched morphology emerges in the XY oriented map, with grains forming square clusters in line with the 90° rotation scan strategy. There are larger grains where the center of the tracks overlap, and finer grains toward the track edges, which is consistent with a cross-section of the microstructure observed in the XZ direction. The slight increase in overlap associated with the 60 μm hatch spacing produces a microstructure with stronger texture, with grains not directly within the {001}<100 > cube alignment coalescing near that texture as opposed to being more randomly distributed, as seen in the 80 μm hatch spacing. Clear column boundaries are absent from the XZ oriented EBSD map, and the XY lacks discernible features from the laser track history. Despite these microstructural changes, the alteration in hatch spacing doesn't appear to impact the melting mode. This shift in texture is attributed to the amplified thermal energy imparted onto the material from the increased overlap, which enhances remelting of previous layers and tracks. As a result, the grain solidification begins to grow from these remelted areas.

17 – 4 PH and CoCrMo specimens were produced using the same parameters for the IN 718 specimens in Fig. 7 and are presented in a consistent manner in Fig. 8 and Fig. 9, respectively, with only the MRD scale bars altered to ensure suitable contrast. The specimens for both materials display comparably high relative densities and low S_a values. For the 17 – 4 PH specimens the 60 μm specimen has a 99.98% relative density and 7.84 μm S_a, while the 80 μm specimen measures 99.97% and 9.94 μm. The CoCrMo 60 μm specimen has a 99.99% relative density and 6.22 μm S_a, while the 80 μm specimen measures 99.97% and 6.85 μm. The FFTs do not produce a noticeable peak at the hatch spacing frequency for either material’s 60 μm specimen but do for both 80 μm specimens, the same trend observed for IN 718. The change in hatch spacing doesn't induce any discernible alteration in the melting mode. Specimens of all three materials exhibit discernible surface ripples at the location of the laser tracks, referred to as laser path ripple, which will be explored separately in the following section.

EBSD results for 17 – 4 PH in Fig. 8 share the same general trends observed previously for IN 718 in Fig. 7. The XZ microstructure of the 80 μm specimen is consistent with those in Fig. 5 (a) and (b), produced using 140 W and 700 mm/s and 200 W and 1000 mm/s, as the laser power and scan speed used to produce this specimens falls between them. The cross-hatched 90° scan rotation strategy is clearly defined in the grain structure of the 80 μm hatch specimen when viewed on the XY cross-section. While the track-width columnar morphology in XZ and cross-hatched square morphology in XY are weakened in the 17 – 4 PH 60 μm hatch spacing specimen, they are still visibly present unlike their complete disappearance in the IN 718 specimen.

The slight increase in track overlap with the 60 μm spacing produces a notably stronger {001}<100 > cube texture than observed for the 80 μm spacing, which is nearly un-textured, with the maximum MRD values increasing from 2.28 to 6.43 in the XY map, and 3.54 to 6.85 in the XZ map. The discrepancy between the XY and XZ EBSD-derived textures for the 80 μm hatch spacing specimen is due to a sampling artifact that can occur when cross-sectioning microstructures with periodic variations in the direction perpendicular to the sampled section. The XZ section acquired is consistent with a cross-section near the center of a track, and oversamples (as a volume percentage) the larger and more oriented grains at the center of the square column morphology, and under samples the smaller more randomly oriented grains near the track edges. The texture derived from the XY aligned EBSD map therefore presents a more accurate approximation of the bulk texture of the specimen, which would be best established using X-ray or neutron diffraction when of critical importance.

Observations of the CoCrMo EBSD maps in Fig. 9 parallel those made for the IN 718 and 17 − 4 PH datasets in Fig. 7 and Fig. 8, where the reduction in hatch spacing from 80 μm to 60 μm breaks up the square columnar morphology and lead to a stronger {001}<100 > cube texture. In both trends the CoCrMo results fall between the other two samples in magnitude, with the square columnar morphology breaking up more than in 17 − 4 PH but less than the IN 718, and the increase in texture strength (best assessed from the XY EBSD) is less than seen in 17 − 4 PH but more than in IN 718.

Modification of the hatch spacing prompts significant changes in both grain morphology and crystallographic texture across all three materials. These changes correlate to the presence of surface features that are discernible through the FFT but not the S_a summary parameter. Together the results in this section show that FFT analysis can be used to non-destructively provide insights into part quality and make processing parameter adjustments once correlations between the parameter space and surface topology have been established for a material.

c. Laser path ripples and melt pool behavior

FFT analysis has proven to be an effective tool for characterizing surfaces and differentiating between parts with distinct melting behaviors, varying part qualities, and even surfaces displaying comparable summary roughness parameters. Analysis of the micro-scale laser path ripple morphology provides a different but complementary approach to distinguish between melting behaviors and explore the intricacies of melt pool formation. The CoCrMo specimens featured in Fig. 10 were produced by adjusting the laser power (90W, 125W, 160W, 195W) and scan speed (840 mm/s, 1200 mm/s, 1560 mm/s). The hatch spacing was held constant at 80 μm. Conduction melting mode is evident from the characteristic semi-circular track morphology in the specimens featuring lower power and higher scan speeds, corresponding to lower VED values.

The CoCrMo specimens in Fig. 10 encompass a range of part qualities, with the lowest VED value (lowest laser power and highest scan speed) exhibiting a relative density of 79.55%. In contrast, the two specimens featuring the highest VED values (highest laser power and lowest scan speed) showcase relative densities of 99.84%. Part density clearly corresponds to changes in the surface condition that

can be described by summary parameters like S_a or FFT analysis, as discussed in the previous section. At a smaller spatial scale, however, there is an observable pattern of laser track ripples within the melt pool that are a consequence of Marangoni flow oscillations. The ripple geometry changes as the parameters shift, just like the variations in larger scale surface topology and relative density. As VED increases—either through higher laser power or reduced scanning speed—the round shape of the laser path ripple evolves from a circular tail into an acutely angled pattern. Notably, the angle of this pattern becomes more acute as VED continues to rise. This shift in pattern signifies the transition in melting mode, moving from conduction mode melting to the establishment of a stable melt pool formation that yields high-density parts. This laser track ripple feature serves as an additional means of identifying how processing parameters impact the melting behavior, and ultimately the likely properties of a part, via non-destructive characterization of the surface. An example of a laser ripple angle is highlighted using a white dashed line in Fig. 10 for the sample fabricated using 195 W laser power and 840 mm/s scan speed.

The significance of the laser ripple angle as a potential part quality metric becomes evident when comparing it to summary parameters like S_a, which is correlated with relative density in Fig. 11 (a) and in previous studies [1], [3]. Figure 11 (b) and (c) displays the angles extracted from the laser ripple patterns in Fig. 10, alongside their relative density and S_a values, respectively. A clear linear correlation is apparent between the laser ripple angles extracted from Fig. 10 and their respective S_a values, with an R^2 value of 0.85. When plotting the relative density as a function of both S_a and the laser ripple angle, however, it appears that the laser ripple angle outperforms the more conventional S_a measurement as a predicter of the high-density processing window and the critical transition from conduction mode melting to a stable melt pool formation. The laser ripple angle vs density plot has notably less scatter and a much sharper high relative density threshold, at about 80°, than the comparable S_a plot. The large error bars observed in the ripple angle measurements reflect both the variety of ripple angles in the height maps and the difficulty of manually capturing these measurements, particularly for the round shaped ripple geometry. However, the two red data points in each plot of Fig. 11 have smaller error bars for each of the three metrics and lower ripple angles than the other specimens. These two specimens represent high quality specimens from this dataset and the reduced error in the ripple angle measurement indicate stability during the melting process. It is noteworthy that the specimens in Fig. 10 did not contain parameter sets with high enough VED to produce unstable keyhole mode parameters where it is expected that the laser ripple angle would continue to decrease as porosity content increases.

Confocal height maps of specimens from all three materials are presented in Fig. 12, with a waveform reduction performed to eliminate the curvature stemming from the laser tracks and visually amplify the laser track ripples. These specimens were printed at four different laser powers using the same hatch spacing (80 μm) and scan speed (840 mm/s). The waveform reduction applied amplifies the laser track ripples for all materials, even for specimens with notably nonuniform surfaces. The lower power specimens experience the typical intertrack undulation seen in conduction mode melting. This phenomenon affects the ripple patterns in such a way that it generates inconsistent laser ripple angles

and non-continuous paths. These track discontinuities lead to the oscillation pointing towards the direction of laser movement, instead of away from it, signaling the end of a melt pool. A new melt pool subsequently forms again, resulting in a laser ripple angle oriented in the correct direction before starting to close once more. These closing melt pools align with the valleys of intertrack undulation. These reverse direction oscillations were not measured when determining the ripple angle. As laser power is increased and the melt pool stabilizes, the formation of laser path ripples becomes uniform with no interruptions.

Slight variations in track formation and laser ripple intensity between the three materials points to material-specific melting behavior. This becomes more apparent when looking at the IN 718 specimens. While several laser ripples with measurable angles are observable for the 90 W and 125 W specimens, these ripple angles cannot be directly measured as laser power continues to rise as IN 718 has a wider melt pool compared to the other alloys and overlap of laser tracks obscures the angle. In the case of overlap the ripple angle can still be interpolated to some extent from one side of the track, and it’s evident that the IN 718 specimens are producing uniform and consistent melt pool geometries. This evidence suggests that the observed ripples pertain to the geometry and health of the melt pool formed during fabrication.

Cross-sectional microscopy of the tracks, shown in Fig. 12 help to elucidate the relationship between the laser ripple angle and the melt pool behavior. Semi-transparent boxes with dashed red lines are used to highlight specific sections on individual 17 – 4 PH specimen surfaces in Fig. 12. These sections are magnified in the images to the right, revealing the changes in post-mortem melt pool dynamics. More acute laser ripple angles are hypothesized to arise from elongation of the melt pool length and are therefore directly tied the increase in VED, which is directly related to the laser power if the scan speed and other parameters are held constant. Prior research has established that higher laser power leads to a deeper and wider melt pool [29]. This widening of the melt pool is observable on the surface, as the point of the ripple or tail of the melt pool becomes increasingly overlapped, and the increased melt pool width and depth are evidenced by the etched cross-sectional micrographs. The dashed black lines indicate the lower boundary and approximate width of the melt pool in the cross-sectional images. The extended duration of melt pool life is due to increased laser power producing a larger thermal mass through both the increased energy and vapor depression effects. This larger thermal mass takes longer to solidify, progressing from the melt pool boundary inward and upward. Ultimately, this process locks in the Marangoni ripples created, with the tip of the angle being hypothesized as the first solidified portion on the trailing side of a traveling melt pool. This surface artifact therefore offers insight into the length, width, and depth of the melt pool.

4. Discussion

The Gelsight data in Fig. 2 reveals that when large-scale surface features are evenly distributed across the top surface, smaller regions observed via a higher-resolution technique such as confocal microscopy offer a reasonable representation of the wider specimen's top surface, with the exception of edge

effects. Everton et al. [30] previously proposed using a smaller, high-resolution areas to represent larger sample regions, a notion that finds support in these findings. The confocal height maps prove highly effective in not only capturing macro-scale surface features but also resolving smaller surface details, such as inter-track defects and the laser path ripples. This method appears well-suited for surface characterization in steady-state regions and for studies establishing the effects of varying processing parameter sets, as are required for qualification of new materials, machines or scanning strategies. Further work is required to determine the efficacy of this method at characterizing non-steady state fabrication zones, and specimens with differing geometries or scanning strategies that may not be adequately represented by smaller areas.

FFT analysis is proven in this study to be a valuable tool for distinguishing between parts that exhibit different melting behaviors, even when they have similar conventional summary parameter values. Figure 3 is an excellent illustration that similar S_a values do not always equate to similar part quality, as S_a fails to discriminate between surface variations in these particular height maps that covey significant information about the melting modes and consequentially the porosity of the samples. In contrast, FFT analysis excels in breaking down these unique surfaces into their respective periodically sized defects and is able to distinguish between them. Identifying high amplitude peaks at key spatial frequencies proves to be an exemplary method for identifying the melting mode and assessing differences between parameter sets. The confocal height maps and associated FFTs presented from Fig. 2 to Fig. 6 reveal distinct surface formations associated with a spectrum of melting modes, ranging between unstable keyhole mode, stable keyhole mode, transition mode melting, and conduction mode melting. This type of surface characterization enables post-mortem examinations of melting behavior and assists in determination of the underlying physical mechanisms governing melting and solidification. While post-mortem melting mode determination has been explored in prior research, it's important to note that microstructure and single track morphology have traditionally been the primary methods used for that analysis [31].

The novel approach here involves using a final printed specimen surface as a means of determining and analyzing melting behavior. To justify this innovative form of analysis, it is essential to establish a clear link between existing knowledge of melting modes, the surface features they form, and porosity defects. For instance, the well-known defect known as lack of fusion porosity, often associated with conduction mode melting [32], is visibly linked to the semicircular irregular track phenomenon observed in Fig. 3 specimen (b) [8]. The periodic smaller irregularly shaped porosity is also indicative of this type of melting. Stable keyhole mode and transition melting, which tend to result in higher relative density parts, are most commonly associated with a uniform surface morphology [10]. In contrast, unstable keyhole mode, characterized by excessive melting, can lead to the formation of large multi-track protrusions and significant large porosity [3]. These findings illustrate the power of FFT analysis in establishing connections between melting modes and the resulting surface characteristics.

Figure 4 to Fig. 6 depict surface height maps, FFT analysis, and EBSD for three different materials with specimens in the high relative density process window. All three specimens in each were produced with

the same VED value but featured proportionally different laser power and scan speed settings. Different surface artifacts, such as surface protrusions and laser track periodicity, are brought on by subtle shifts in melting mode and captured by the FFT analysis. The corresponding EBSD maps reveal slight differences such as defined microstructural columns linked to laser track stability and subtle shifts in the crystallographic texture, but ultimately the microstructures between the specimens are similar. Here the FFT analysis provides valuable information not solely about the part quality itself, but by capturing changes to the melting mode behavior it signals how close the parameter set is to falling outside the effective processing window. LPBF part qualification is of interest to many industries as is parameter set design, and aiming for a parameter set in the center of the process window can help account for the stochastic aspects of processing and more resilience to process anomalies. As the surface is readily available data during fabrication, this type of analysis also opens up avenues for *in situ* monitoring surface characterization to ensure the process remains within acceptable limits. It is well known that altered parameters have an effect microstructural characteristics of materials [33], [34], [35], however a comprehensive study of this kind has not been done within the high relative density process window. The length and time scales of confocal laser scanning microscopy are not realistic for most *in situ* applications, but alternative solutions such as laser speckle pattern analysis [36] that can periodic features of the surface may have sufficient resolution combined with rapid data acquisition to allow for the generation of the required data set for application purposes.

The results presented in Fig. 7 to Fig. 9 underscore the significant impact of certain process parameters on microstructural texture preferences. It is evident that adjusting the hatch spacing can lead to detectable surface changes as observed in the associated FFTs, while maintaining a high relative density. Across all three materials examined, the FFT results reveal a noteworthy trend. In the case 60 µm hatch spacing specimens, there is no discernible frequency peak at the hatch spacing value, whereas the 80 µm hatch spacing specimens exhibit a frequency peak at this specific value, capturing the shift in melt pool overlap. Furthermore, a reduction in hatch spacing for all materials results in an increased crystallographic {001}<100 > cube texture. Such shifts in orientation are a consequence of increased overlap, resulting in a shift in thermal gradient and a different seed of grains at the melt pool boundary during solidification. A similar phenomenon, involving control of thermal gradient, was observed in a previous study employing electron beam melting [37].

A further use of the surface as an indicator of melting behavior, in addition to FFT analysis, was illustrated with characterization of laser path ripples. The shape and characteristics of these laser path ripples have been observed to undergo changes in response to alterations in processing parameters, which correlate with shifts in the melting mode from conduction to stable transition or keyhole melting modes, as depicted in Fig. 10. This observation aligns with findings from a prior study [38]. It is noteworthy that laser track ripples, akin to those commonly observed in welding [9], have been documented in previous L-PBF studies utilizing single laser tracks [39]. These ripples have been attributed to the interplay of Marangoni flow and recoil pressure, both of which are influenced by the input process parameters and are therefore valuable indications of the process behavior. This is

supported in Fig. 11, which demonstrates that laser path ripple angle not only correlates to the S_a value but is a better predictor of the relative part density than the S_a value.

A more in-depth examination of this surface artifact could offer insights into the improvement of melt pool simulation studies, particularly its potential connection to melt pool length. By employing the equations provided by Tang et al. [40], the melt pool length can be estimated. In the case of the specimens presented in Fig. 12, the calculations reveal that as laser power increases and the laser ripple angle decreases, the melt pool length increases. This result aligns with expectations, as a longer melt pool naturally requires a smaller angle to intersect at the edges spanning the width of the melt pool. This suggests that a quick measurement of melt pool width and the angle of the laser path ripples may serve as a valuable method for validating simulated melt pool dimensions. However, it is essential to acknowledge the limitations of this metric. Notably, the presence of laser ripples is a prerequisite for measurement. For instance, the IN 718 specimens in this study did not exhibit measurable laser ripple angles, as is evident from Fig. 7. Additionally, in Fig. 8 and Fig. 9, where the hatch spacing was reduced to 60 μm, no intertrack angle was observed. Instead, the visible ripples were generated when adjacent tracks overlapped during the fabrication process, erasing a measurable intertrack ripple angle. While there are limitations to consider, these findings shed light on the potential of laser path ripples as a valuable indicator of process behavior that can contribute to the advancement of L-PBF.

5. Conclusion

This study demonstrates the potential of new surface characterization techniques to be valuable tools for distinguishing between parts that exhibit different melting behaviors using laser powder bed fusion (L-PBF). IN 718, 17 – 4 PH stainless steel, and CoCrMo alloys were fabricated using L-PBF, and height maps of the top surface were generated for each specimen using high-resolution confocal laser scanning microscopy. The findings demonstrate the remarkable effectiveness of 1-D fast Fourier transform (FFT) profiles in distinguishing parts with varying relative densities, similar S_a values, and differing melting modes. Notably, the presence of high-amplitude peaks at specific spatial frequencies revealed unique surface characteristics linked to melting modes and ideal process behavior, a capability that conventional summary parameters lack.

The FFT method proved valuable in discerning changes in crystallographic textures resulting from alterations in parameters, such as hatch spacing, which has not been proven possible to achieve through summary parameters like S_a and relative density. Additionally, FFT analysis successfully differentiated parts possessing different melting modes and only minor microstructural differences that were within the perceived high relative density process window. This suggests that FFT surface analysis has the potential to revolutionize the amount of process health information that can be extracted through surface characterization, with implications for *in situ* monitoring and on-the-fly parameter editing.

The laser path ripple was observed and measured, represented as a laser ripple angle. This angle correlates with the broader process health metric of S_a, and when measurable appears to be a better and

more sensitive predictor of the relative part density. It is anticipated that this intertrack feature may also correlate with melt pool geometry, such as melt pool length, making it a valuable tool for validating simulation models.

In summary, this research underscores the limitations of surface characterization using traditional summary parameters in the context of L-PBF manufacturing. It was demonstrated that the L-PBF manufacturing process leaves behind critical post-mortem process behavior signatures on each surface, which were directly correlated with part and process health in our study. This work opens new avenues for enhancing our understanding of L-PBF processes and highlights the potential for advanced surface analysis techniques.

Declarations

The authors declare that they have no known competing financial interests or personal relationships that could have appeared to influence the work reported in this paper.

Author Contributions

All authors contributed to the conceptualization, methodology, and final revision of this article. Material preparation, characterization, formal analysis, and original drafting of this article was preformed by Sean Dobson. Project administration, supervision, and guidance were provided by Ashley Paz y Puente and Matthew Steiner.

Acknowledgements

The authors would like to especially acknowledge Dr. Ryan DeHoff at Oak Ridge National Laboratory for championing this work. Thank you to the materials characterization laboratory team at Oak Ridge National Laboratory, especially Sarah Graham, and Andrès Márquez Rossy for guidance on specimen characterization. Thank you to the team at the University of Louisville Additive Manufacturing Institute of Science and Technology (AMIST), especially Gary Graff and Dr. Sundar Atre, for assistance with specimen fabrication. Thank you to Dr. Eddie Schwalbach for the helpful conversations regarding the laser path ripple data.

References

1. Balbaa M, Mekhiel S, Elbestawi M, McIsaac J (2020) On selective laser melting of Inconel 718: Densification, surface roughness, and residual stresses. Mater Design 193:108818
2. Kamath C, El-Dasher B, Gallegos GF, King WE, Sisto A (2014) Density of additively-manufactured, 316L SS parts using laser powder-bed fusion at powers up to 400 W. Int J Adv Manuf Technol 74:65–78

3. Wang D, Liu Y, Yang Y, Xiao D (2016) Theoretical and experimental study on surface roughness of 316L stainless steel metal parts obtained through selective laser melting. Rapid Prototyp J
4. Yonehara M, Kato C, Ikeshoji T-T, Takeshita K, Kyogoku H (2021) Correlation between surface texture and internal defects in laser powder-bed fusion additive manufacturing. Sci Rep 11(1):22874
5. Senin N, Thompson A, Leach R (2018) Feature-based characterisation of signature topography in laser powder bed fusion of metals. Meas Sci Technol 29(4):045009
6. Fabbro R, Hamadou M, Coste F (2004) Metallic vapor ejection effect on melt pool dynamics in deep penetration laser welding. J Laser Appl 16(1):16–19
7. Ladani L, Romano J, Brindley W, Burlatsky S (2017) Effective liquid conductivity for improved simulation of thermal transport in laser beam melting powder bed technology. Additive Manuf 14:13–23
8. Zhou X et al (2015) 3D-imaging of selective laser melting defects in a Co–Cr–Mo alloy by synchrotron radiation micro-CT. Acta Mater 98:1–16
9. Hu J, Guo H, Tsai HL (May 2008) Weld pool dynamics and the formation of ripples in 3D gas metal arc welding. Int J Heat Mass Transf 51(9):2537–2552. 10.1016/j.ijheatmasstransfer.2007.07.042
10. Zhao C et al (2022) Laser melting modes in metal powder bed fusion additive manufacturing. Rev Mod Phys 94(4):045002
11. Assuncao E, Williams S, Yapp D (2012) Interaction time and beam diameter effects on the conduction mode limit. Opt Lasers Eng 50(6):823–828
12. Cunningham R et al (2019) Keyhole threshold and morphology in laser melting revealed by ultrahigh-speed x-ray imaging. Science 363(6429):849–852
13. Lee JY, Ko SH, Farson DF, Yoo CD (2002) Mechanism of keyhole formation and stability in stationary laser welding. J Phys D 35(13):1570
14. Khairallah SA, Anderson AT, Rubenchik A, King WE (2016) Laser powder-bed fusion additive manufacturing: Physics of complex melt flow and formation mechanisms of pores, spatter, and denudation zones. Acta Mater 108:36–45
15. Alrbaey K, Wimpenny D, Tosi R, Manning W, Moroz A (Jun. 2014) On Optimization of Surface Roughness of Selective Laser Melted Stainless Steel Parts: A Statistical Study. J Mater Eng Perform 23(6):2139–2148. 10.1007/s11665-014-0993-9
16. Yu W, Sing SL, Chua CK, Tian X (2019) Influence of re-melting on surface roughness and porosity of AlSi10Mg parts fabricated by selective laser melting. J Alloys Compd 792:574–581
17. Mishra AK, Kumar A (2020) Effect of surface morphology on the melt pool geometry in single track selective laser melting, *Materials Today: Proceedings*, vol. 27, pp. 816–823
18. Qiu C, Panwisawas C, Ward M, Basoalto HC, Brooks JW, Attallah MM (2015) On the role of melt flow into the surface structure and porosity development during selective laser melting. Acta Mater 96:72–79

19. Fleming TG, Nestor SG, Allen TR, Boukhaled MA, Smith NJ, Fraser JM (2020) Tracking and controlling the morphology evolution of 3D powder-bed fusion in situ using inline coherent imaging. Additive Manuf 32:100978
20. DePond PJ et al (Sep. 2018) In situ measurements of layer roughness during laser powder bed fusion additive manufacturing using low coherence scanning interferometry. Mater Design 154:347–359. 10.1016/j.matdes.2018.05.050
21. Dong W, Stout K (1995) Two-dimensional fast Fourier transform and power spectrum for surface roughness in three dimensions, *Proceedings of the Institution of Mechanical Engineers, Part B: Journal of Engineering Manufacture*, vol. 209, no. 5, pp. 381–391
22. Bruel, Kjaer (1983) Surface Roughness Analysis. Tech Rev, vol. No. 3
23. Zeng Q, Qin Y, Chang W, Luo X (2018) Correlating and evaluating the functionality-related properties with surface texture parameters and specific characteristics of machined components, *International Journal of Mechanical Sciences*, vol. 149, pp. 62–72, Dec. 10.1016/j.ijmecsci.2018.09.044
24. Tang C, Le KQ, Wong CH (2020) Physics of humping formation in laser powder bed fusion. Int J Heat Mass Transf 149:119172
25. Kunze K, Etter T, Grässlin J, Shklover V (Jan. 2015) Texture, anisotropy in microstructure and mechanical properties of IN738LC alloy processed by selective laser melting (SLM). Mater Sci Engineering: A 620:213–222. 10.1016/j.msea.2014.10.003
26. Geiger F, Kunze K, Etter T (Apr. 2016) Tailoring the texture of IN738LC processed by selective laser melting (SLM) by specific scanning strategies. Mater Sci Engineering: A 661:240–246. 10.1016/j.msea.2016.03.036
27. Zhou X et al (May 2015) Textures formed in a CoCrMo alloy by selective laser melting. J Alloys Compd 631:153–164. 10.1016/j.jallcom.2015.01.096
28. Wan HY, Zhou ZJ, Li CP, Chen GF, Zhang GP (2018) Effect of scanning strategy on grain structure and crystallographic texture of Inconel 718 processed by selective laser melting, *Journal of Materials Science & Technology*, vol. 34, no. 10, pp. 1799–1804, Oct. 10.1016/j.jmst.2018.02.002
29. Dilip J et al (2017) Influence of processing parameters on the evolution of melt pool, porosity, and microstructures in Ti-6Al-4V alloy parts fabricated by selective laser melting. Progress Additive Manuf 2:157–167
30. Everton SK, Hirsch M, Stravroulakis P, Leach RK, Clare AT (2016) Review of in-situ process monitoring and in-situ metrology for metal additive manufacturing. Mater Design 95:431–445
31. King WE et al (2014) Observation of keyhole-mode laser melting in laser powder-bed fusion additive manufacturing. J Mater Process Technol 214(12):2915–2925
32. Patel S, Vlasea M (Mar. 2020) Melting modes in laser powder bed fusion. Materialia 9:100591. 10.1016/j.mtla.2020.100591
33. Zhao R et al (2022) On the role of volumetric energy density in the microstructure and mechanical properties of laser powder bed fusion Ti-6Al-4V alloy. Additive Manuf 51:102605

34. Hager EM et al (Mar. 2022) Development of high density parts in the low-alloy, high-performance steel AF9628 using laser powder bed fusion. Mater Sci Engineering: A 838:142656. 10.1016/j.msea.2022.142656
35. Larimian T, Kannan M, Grzesiak D, AlMangour B, Borkar T (Jan. 2020) Effect of energy density and scanning strategy on densification, microstructure and mechanical properties of 316L stainless steel processed via selective laser melting. Mater Sci Engineering: A 770:138455. 10.1016/j.msea.2019.138455
36. Shimizu M, Sawano H, Yoshioka H, Shinno H (Jan. 2014) Surface texture assessment of ultra-precision machined parts based on laser speckle pattern analysis. Precis Eng 38(1):1–8. 10.1016/j.precisioneng.2013.06.005
37. Dehoff RR, Kirka MM, Ellis E, Paquit VC, Nandwana P, Plotkowski AJ (2019) Electron beam melting technology improvements. Oak Ridge National Lab.(ORNL),. Oak Ridge, TN (United States)
38. Schwalbach EJ, Donegan SP, Chapman MG, Chaput KJ, Groeber MA (2019) A discrete source model of powder bed fusion additive manufacturing thermal history. Additive Manuf 25:485–498
39. Tang P et al (2020) The Formation of Humps and Ripples During Selective Laser Melting of 316l Stainless Steel, *JOM*, vol. 72, no. 3, pp. 1128–1137, Mar. 10.1007/s11837-019-03987-7
40. Tang M, Pistorius PC, Beuth JL (Mar. 2017) Prediction of lack-of-fusion porosity for powder bed fusion. Additive Manuf 14:39–48. 10.1016/j.addma.2016.12.001

Figures

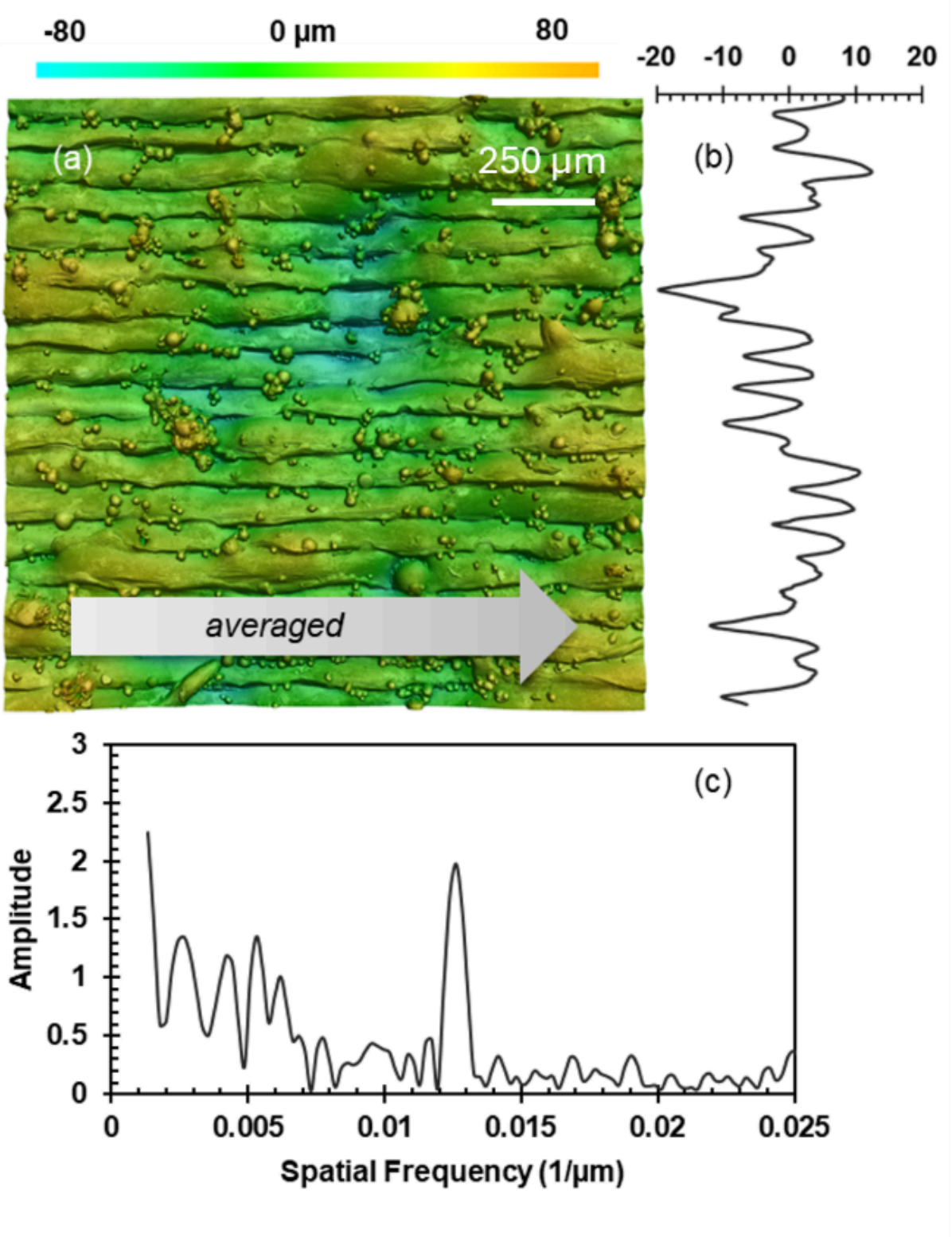

Figure 1

(a) confocal laser scanning 3-D height map, (b) 1-D roughness profile of point cloud data averaged along parallel laser track direction, (c) FFT of 1-D averaged roughness profile.

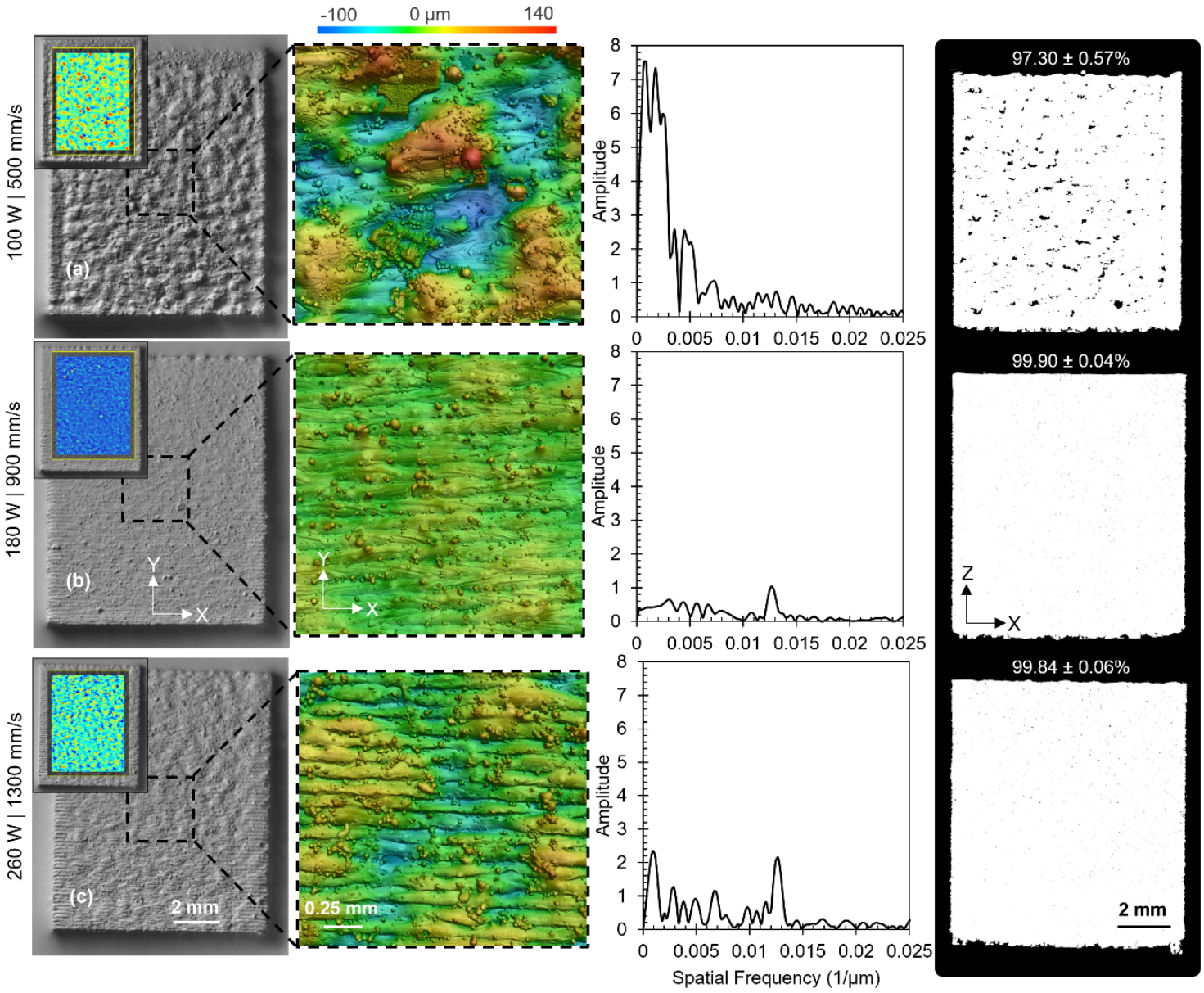

Figure 2

CoCrMo specimens (a), (b), and (c) produced with the same VED using different parameters, with (left to right) Gelsight tactile surface characterization, confocal height maps, 1-D FFT along the y-axis, and a metallographic section with contrast thresholded to highlight porosity.

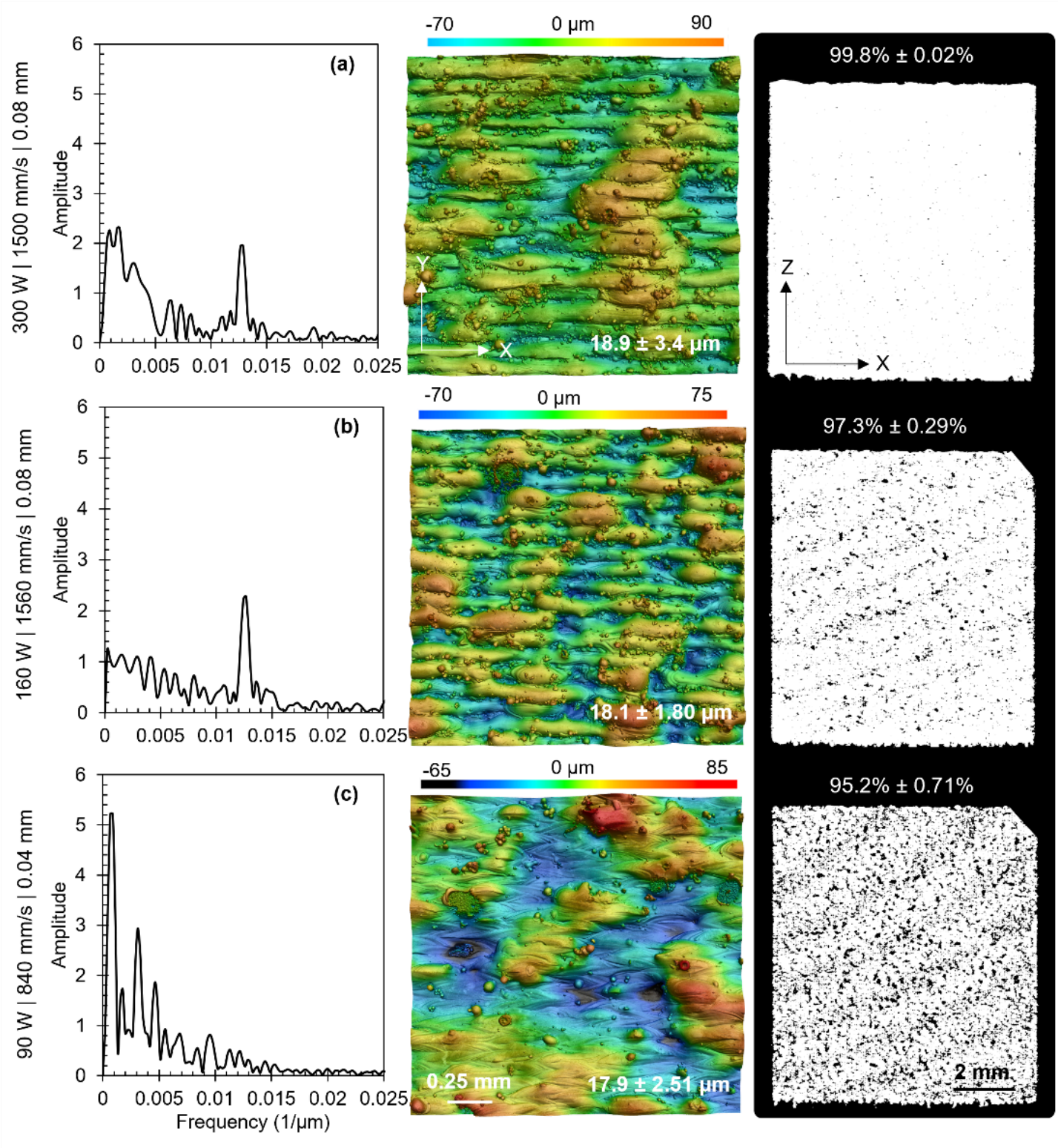

Figure 3

CoCrMo specimens (a), (b) and (c) produced with different parameters but possessing similar roughness values, with (left to right) 1-D FFT along the y-axis, confocal height maps, and metallographic sections with contrast thresholded to highlight porosity.

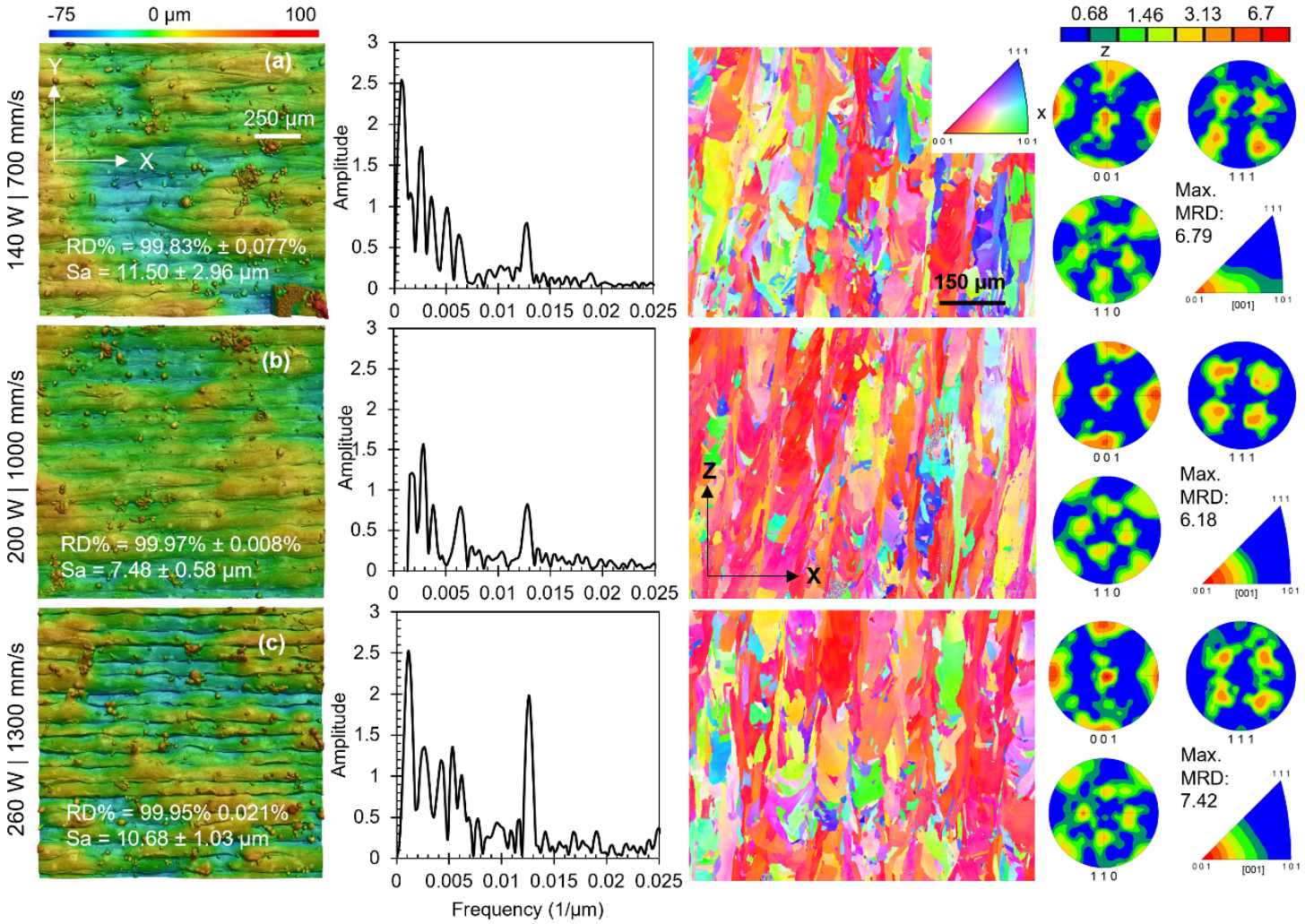

Figure 4

IN 718 specimens (a), (b), and (c) produced with the same VED using different parameters, with (left to right) confocal height maps, 1-D FFT along the y-axis, EBSD maps, and pole and reduced inverse pole figures in MRD scale.

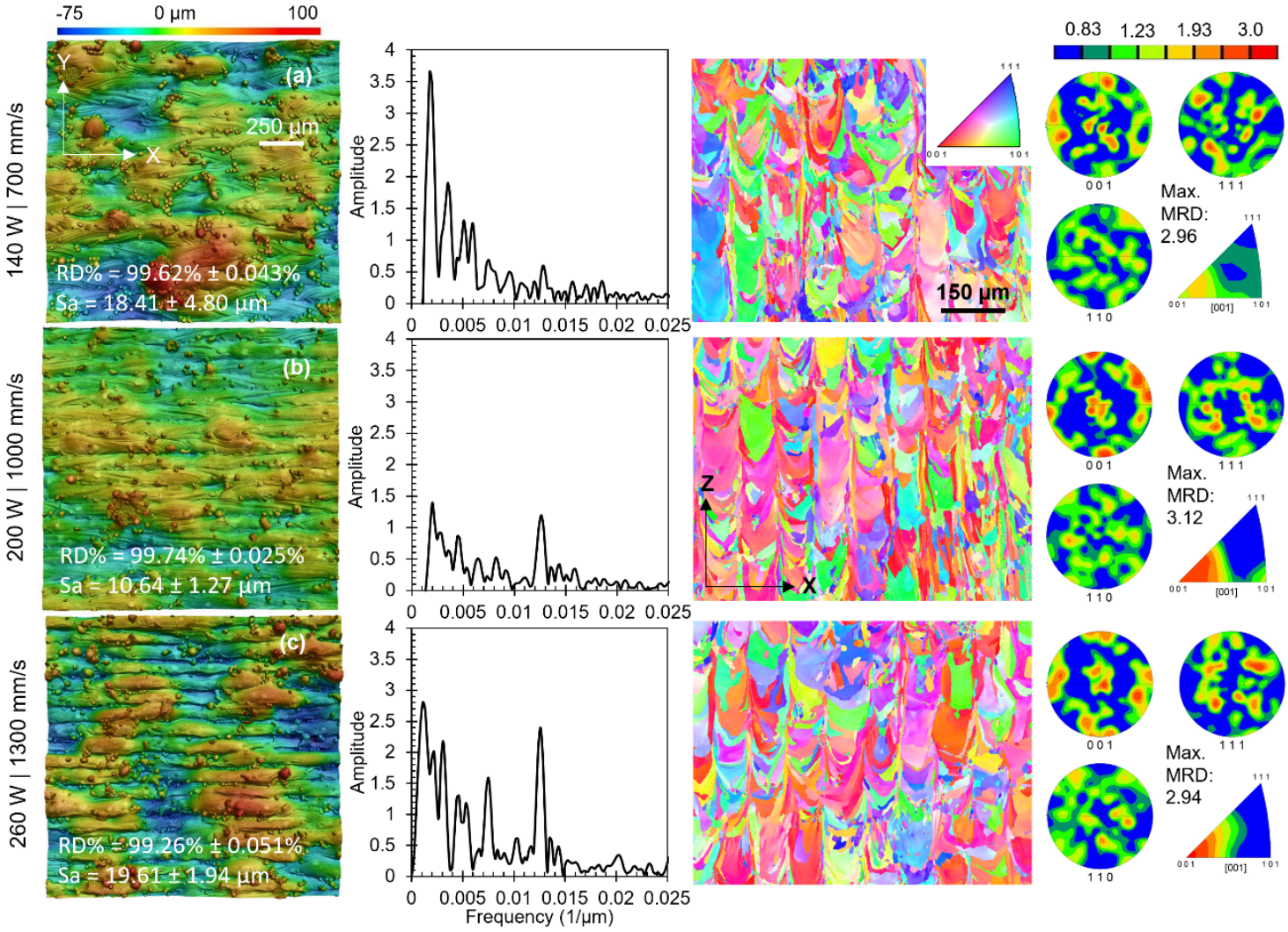

Figure 5

17-4 PH stainless steel specimens (a), (b), and (c) produced with the same VED using different parameters, with (left to right) confocal height maps, 1-D FFT along the y-axis, EBSD maps, and pole and reduced inverse pole figures in MRD scale.

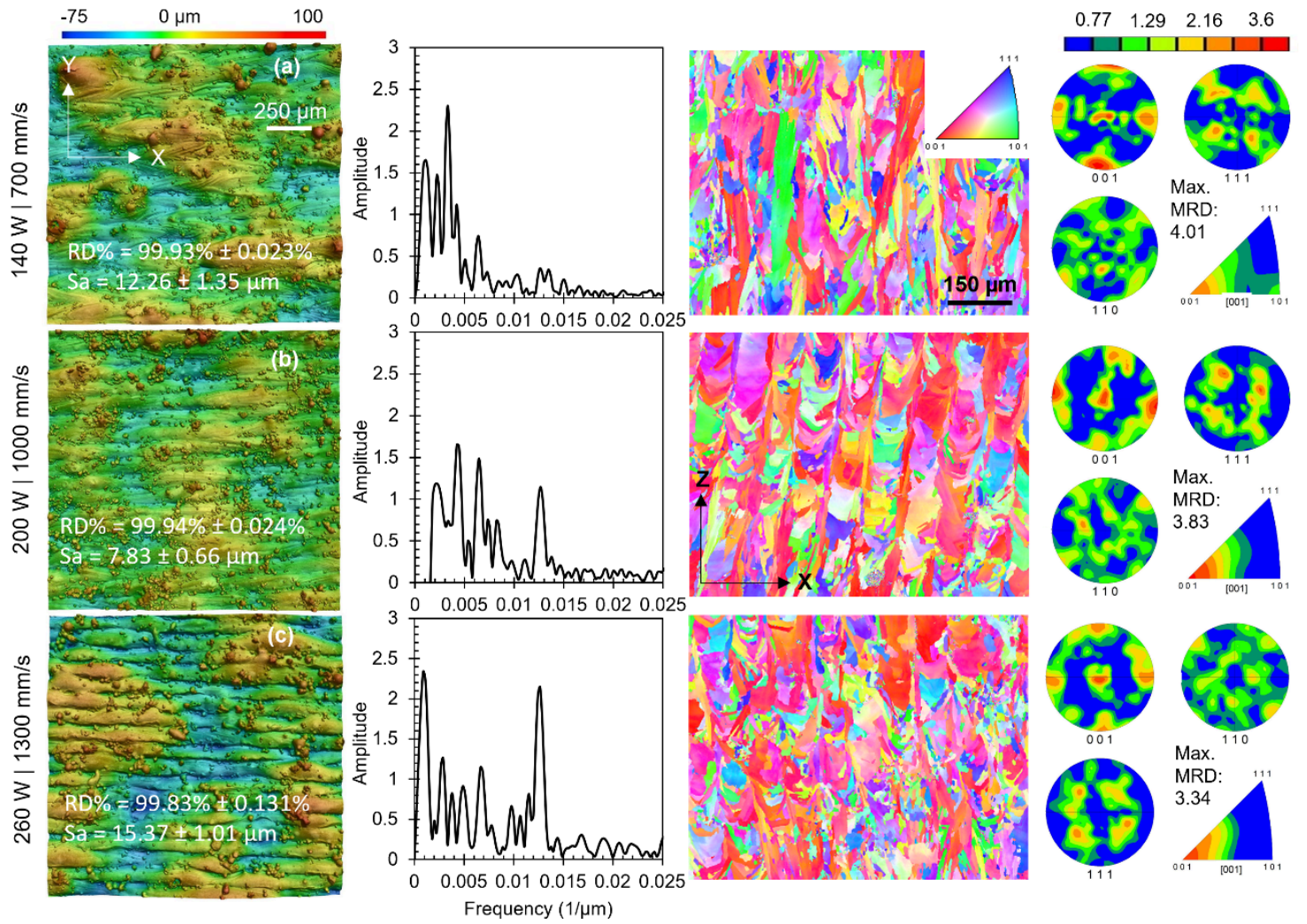

Figure 6

CoCrMo specimens (a), (b), and (c) produced with the same VED using different parameters, with (left to right) confocal height maps, 1-D FFT along the y-axis, EBSD maps, and pole and reduced inverse pole figures in MRD scale.

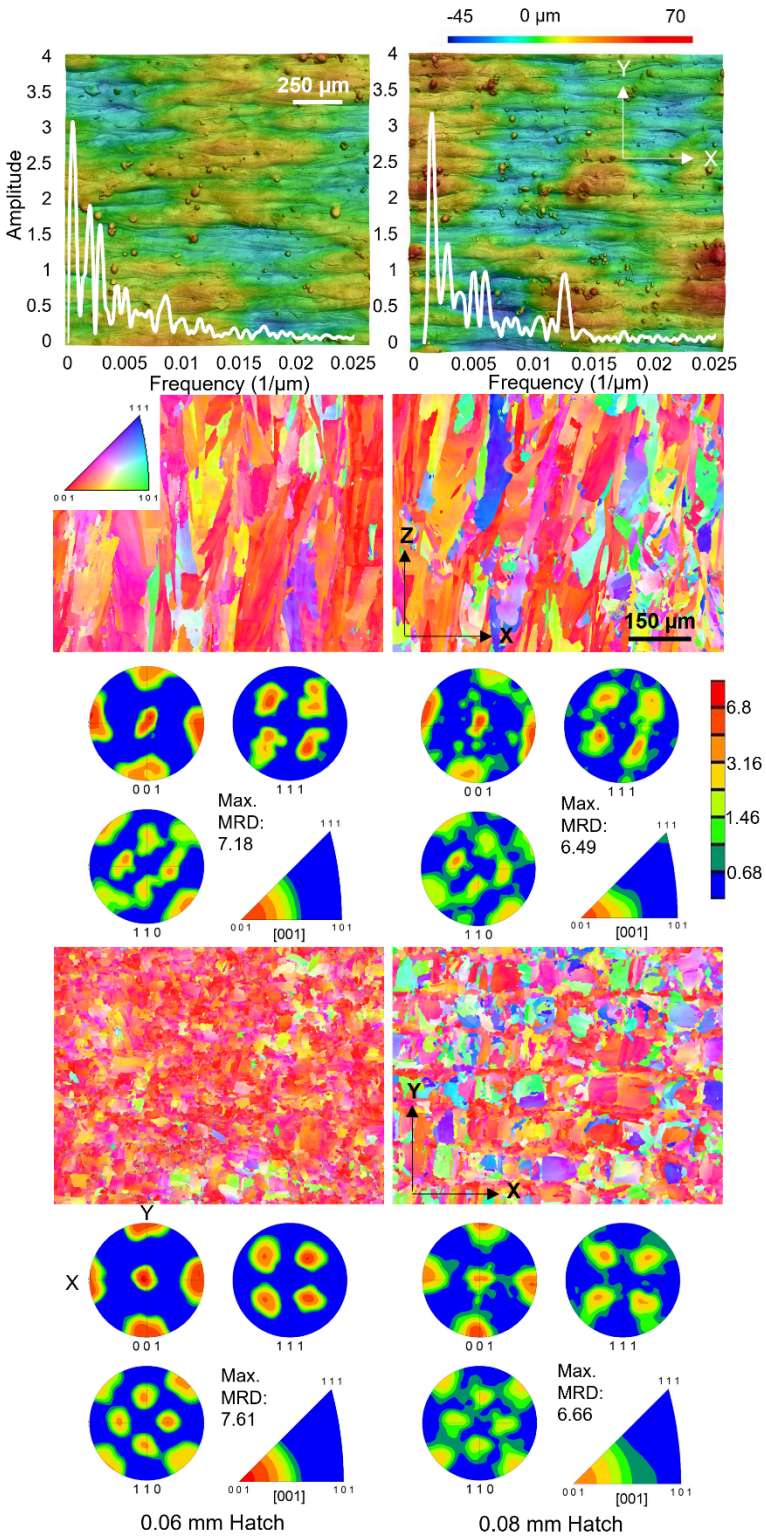

Figure 7

IN 718 specimens (160 W, 840 mm/s) with 60 µm (left column) and 80 µm (right column) hatch spacings. The top row presents confocal height maps overlayed with 1-D FFTs along the y-axis, followed by XZ and XY oriented EBSD maps with pole figures and reduced inverse pole figures located directly below each corresponding map.

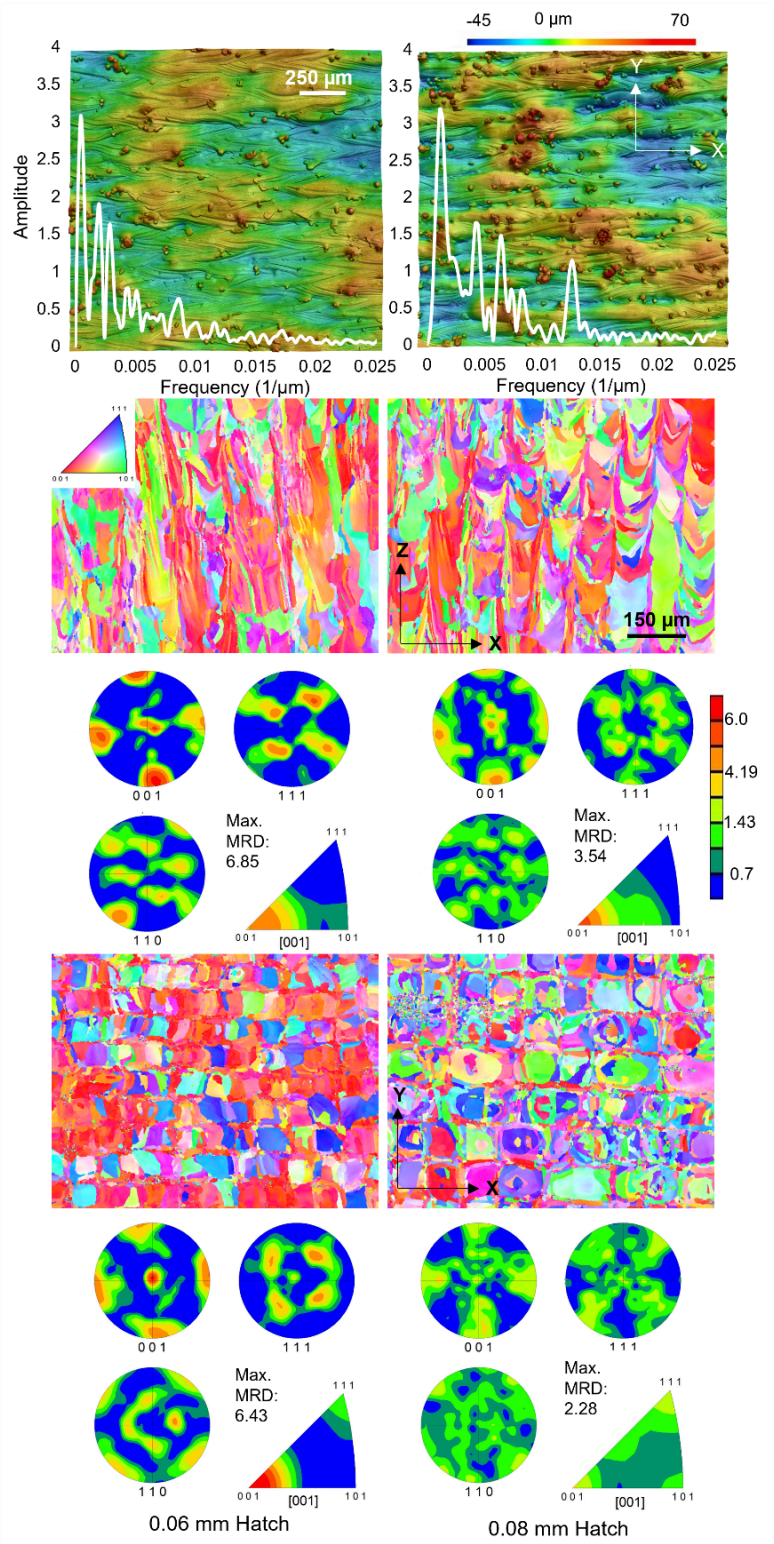

Figure 8

17-4 PH specimens (160 W, 840 mm/s) with 60 µm (left column) and 80 µm (right column) hatch spacings. The top row presents confocal height maps overlayed with 1-D FFTs along the y-axis, followed by XZ and XY oriented EBSD maps with pole figures and reduced inverse pole figures located directly below each corresponding map.

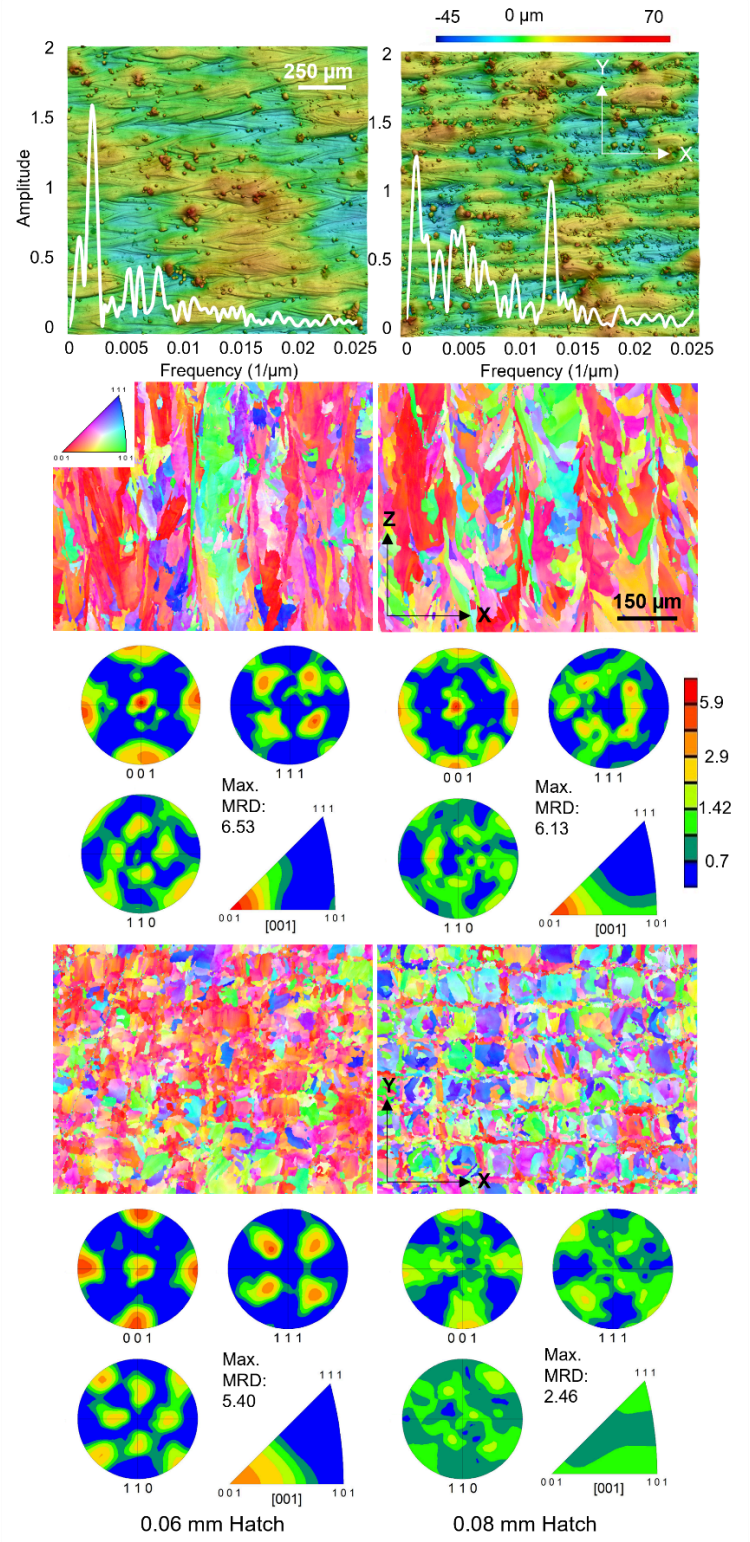

Figure 9

CoCrMo specimens (160 W, 840 mm/s) with 60 µm (left column) and 80 µm (right column) hatch spacings. The top row presents confocal height maps overlayed with 1-D FFTs along the y-axis, followed by XZ and XY oriented EBSD maps with pole figures and reduced inverse pole figures located directly below each corresponding map.

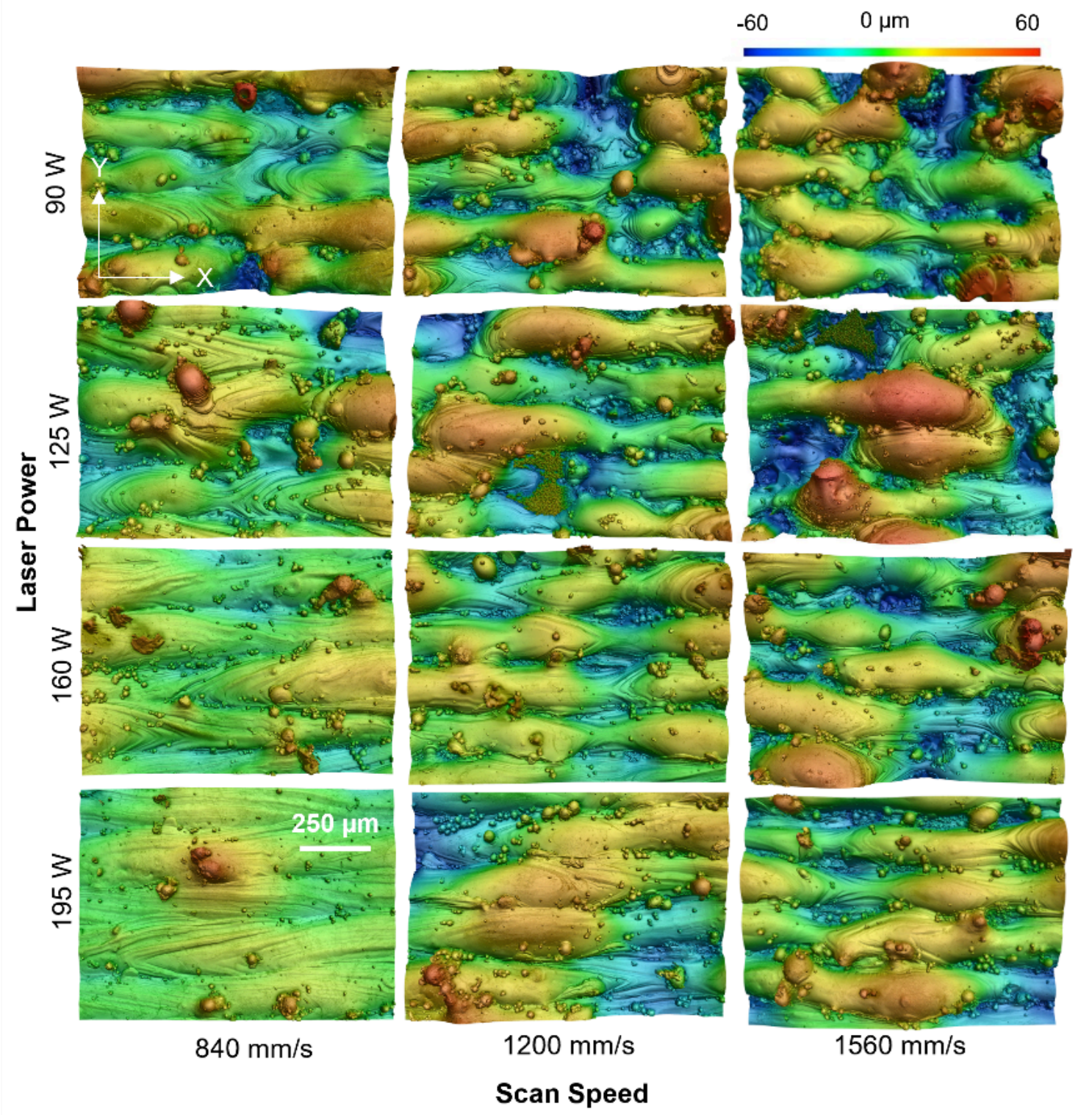

Figure 10

Confocal height maps of CoCrMo specimens with varied laser power and scan speed, 80 µm hatch spacing.

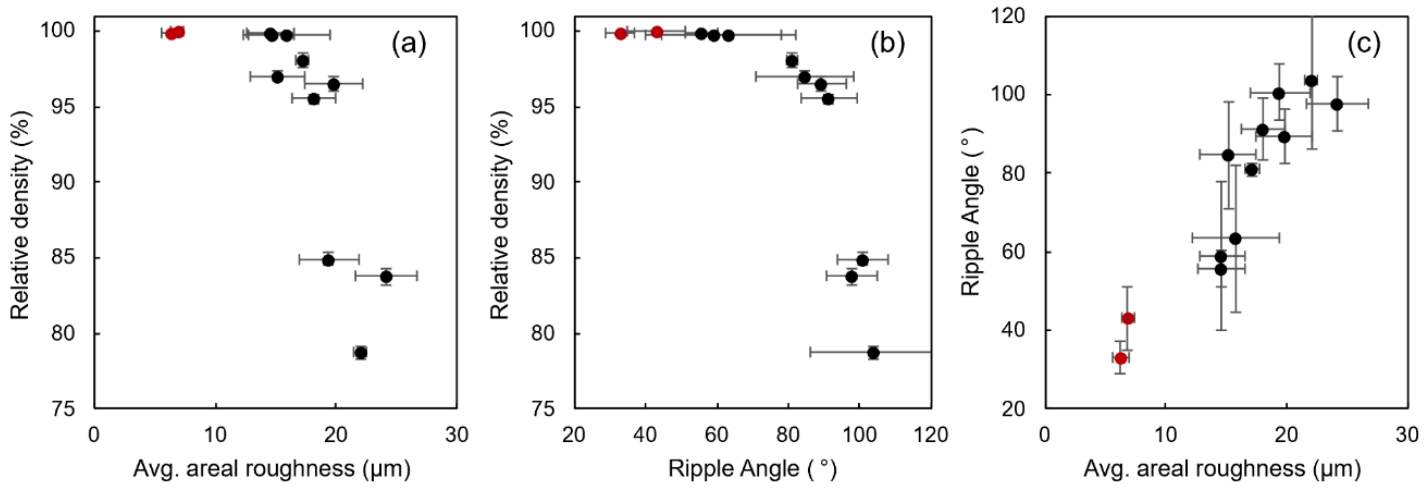

Figure 11

(a) Avg. areal roughness, S_a, plotted along with relative density, (b) laser ripple angle plotted along with relative density, and S_a plotted with laser ripple angle.

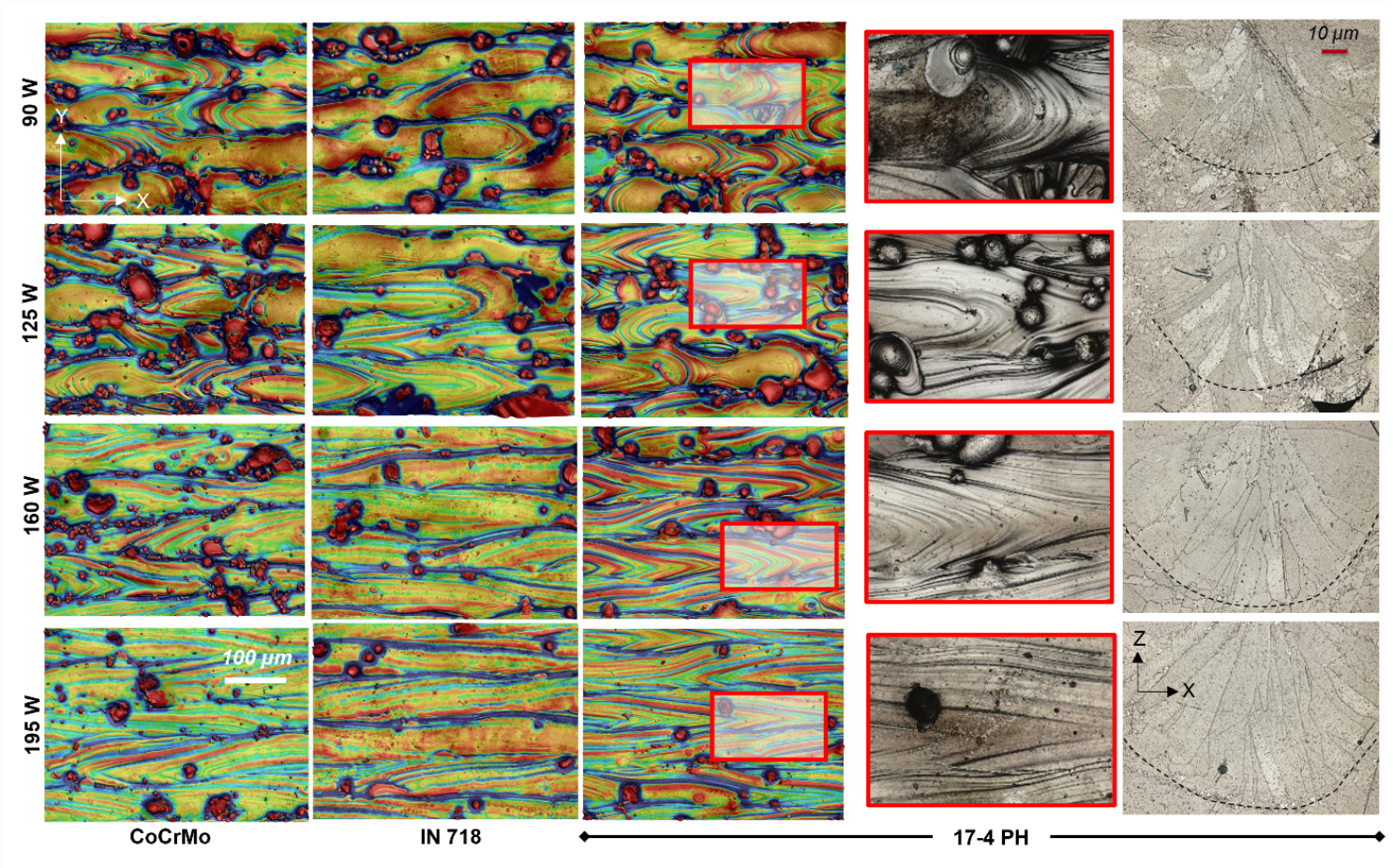

Figure 12

(Left) Waveform reduced micro-confocal height maps of CoCrMo, 17-4 PH, IN 718 specimens with varied laser power with arrows indicating laser path ripples. (Right) Microscopy of etched cross-sections of selected regions of 17-4 PH samples (dashed red boxes) to show the microstructure of the melt pools and approximate melt pool boundaries (dashed black lines)